

Phases Transition Mechanism in the Growth of WS₂ and MoS₂ Layers: Ab Initio Data Driving Machine Learning Molecular Dynamics

Luneng Zhao, Junfeng Gao, Xiaoran Shi, Hongsheng Liu, Jijun Zhao, Feng Ding

Abstract

Accurate and large-scale atomic simulation is crucial for understanding growth mechanism and precise synthesis control of crystals. However, it is beyond the capacities of both *ab initio* and classical molecular dynamics (MD). This study takes a feasible way by developing *ab initio* data to accurate machine learning interatomic potentials (MLIPs) to explore the complex growth processes. It successfully simulated the growth of monolayer, bilayer MoS₂/WS₂ and MoS₂/WS₂ heterostructures under variable conditions. Importantly, a SMMS (M is Mo/W atom) is disclosed as a new 2D structure with high stability during the growth. The two-step vapor-deposition can be regarded as the alternating between MS₂ and SMMS structures. Besides, the intermediate SMMS structure easy forms alloys can result in production of Mo_xW_{1-x}S₂ alloy. Furthermore, metallic SMMS is an ideal self-intercalating electrode for transition metal dichalcogenides based FET. This research provides a mode that *ab initio* data driving MLIPs to efficient and accurate atomic growth simulation and design of materials.

2D materials have significantly advanced condensed matter physics and materials science due to their unique electronic, optical and mechanical properties [1,2]. Among them, transition metal dichalcogenides (TMDCs) have attracted intense attentions due to their suitable band gap and fast carriers [3–11]. The synthesis of high-quality TMDC layers [12,13] and their subsequent integration into heterostructures [14–18] represents a research field of intense scientific and technological investigation. TMDC heterostructures, constituted by the vertical assembly of different TMDC layers, manifest emergent electronic and optical functionalities that are not present in the individual layers [7,19–22]. Optimizing device performance requires mastering TMDC growth processes, as emergent properties critically depend on the layers' interfacial integrity [23].

Established synthesis methods such as chemical vapor deposition (CVD) [1,7,24–28] and molecular beam epitaxy (MBE) [18,29–31] have enabled the precise growth of TMDCs down to monolayer. Recently, a novel two-step vapor-deposition technique was proposed to synthesize high-quality TMDC heterostructures [32]. This method involves the magnetron sputtering of transition metals onto pre-existing TMDC substrates, followed by the deposition of Group VI elements, leading to the chalcogenization of metal atomic layer. The dynamics of this process, especially the post-deposition behavior of transition metals on TMDC substrates, is very complex and full of mystery.

Recently, the development of machine learning interatomic potentials (MLIPs) has revolutionized our ability to capture and model the subtle interplay of atoms in material systems [33–39], by training density functional theory (DFT) data to accurately represent interatomic forces and potential energy surfaces [40–42]. This advancement enables large-scale and high-precision simulations of the complex growth processes, providing insights into the microscopic mechanisms that govern the formation and evolution of materials [43–47].

In this letter, we developed an MLIP based on an Equivariant Graph Neural Network (EGNN) implemented in NequIP package [42], which is proved to have higher data efficiency and exhibit superior generalization performance [42]. We utilized DFT to analyze a broad spectrum of Mo-W-S-hybrid structures. This includes their elemental bulks, different layers of TMDCs, MoS₂/WS₂ heterostructures, and their interactions with both homo- and hetero-metallic clusters, along with S clusters, and the other various configurations of MoWS alloys, as illustrated in Fig. S1(a). These calculations collectively constitute a comprehensive dataset of ~ 26,000. The development of an accurate and reliable MLIP involves a rigorous training and validation process. 80% of the data in the DFT dataset is used as the training set to optimize the parameters of the EGNN, and 20% of the data is used as the test set to monitor the model's performance on unseen data and prevent overfitting.

The parity plot in Fig. S1(b) demonstrates excellent agreement between the MLIP and DFT energies, with a mean absolute error (MAE) of 1.6 meV and a root mean square error (RMSE) of 3.7 meV per atom. Similarly, Fig. S1(c) shows a comparison of the atomic forces, revealing the MLIP well reproduced the DFT forces, with a MAE of 47.9 meV/Å and an RMSE of 101.3 meV/Å. To further validate the capability of our MLIP for simulating the growth of TMDC materials, by implemented in MLIP with molecular dynamics (MLMD). First, a random clusters mixture of Mo, W, and S atoms in a ratio of 1:1:4 were annealing from 1500 K to 900 K lasting 2 ns. An ordered TMDC layers including 2H and 1T phases formed, demonstrating the reliability of our MLIP in modeling complex growth behavior of TMDC (shown in Fig. S2 and Video S1).

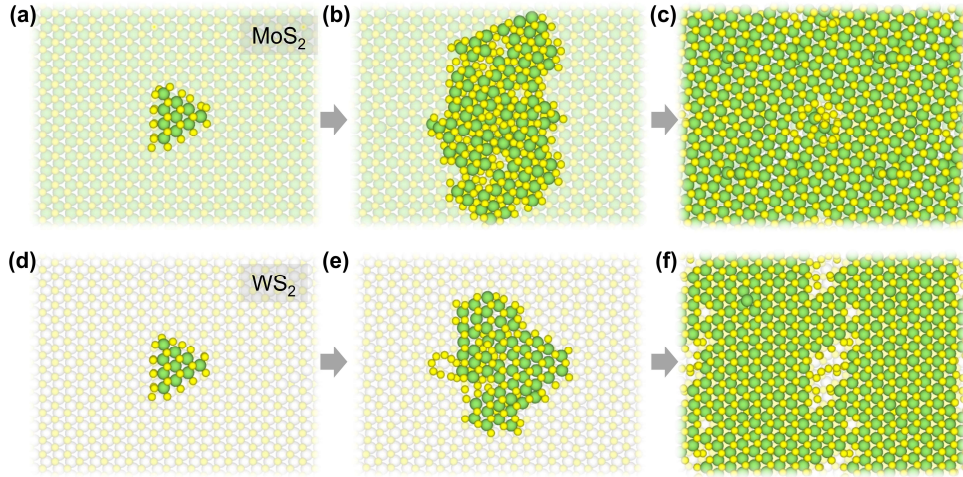


FIG. 1. Sequential MLMD simulations illustrating the growth of a second MoS₂ layer on monolayer substrates of MoS₂ and WS₂. The homogeneous growth MoS₂ on MoS₂: (a) Initial triangular 2H-MoS₂ nucleus, (b) snapshot at 335 ps, (c) the continuous MoS₂ layered forms at 5 ns. The heteroepitaxy growth MoS₂ on WS₂ substrate: (d) Initial 2H-MoS₂ nucleus on the monolayer WS₂, (e) the configuration at 286.9 ps, and (f) continuous growth snapshot at 1.4 ns.

Then, the homogeneous and growth heteroepitaxy of second layer of MoS₂ were both simulated on MoS₂ and WS₂, respectively, by a MLMD simulation at 1100 K with simultaneously adding Mo and S atoms, a process analogous to the growth of MoS₂ via MBE (shown in Video S2 and Video S3). As illustrated in Fig. 1(a), the simulation commenced with a triangular 2H-MoS₂ nucleus placed on the monolayer 2H-MoS₂ surface to represent the nucleation at the onset of growth. Mo and S atoms were deposited onto the surface at a specific rate of 516 picoseconds per layer. Fig. 1(b) illustrates the system at 335 picoseconds, highlighting the evolving growth process. At this juncture, the second layer of MoS₂ had grown significantly and began to exhibit characteristics of the 1T phase. After 1032 picoseconds, the addition of Mo atoms and S atoms was stopped, and the entire system relaxed at 1100 K. After 5 ns of simulation, the growth of the second layer of MoS₂ has been basically completed and shows the characteristics of the 2H phase, as shown in Fig. 1(c). The 1T phase in the early state mostly disappears indicating that MoS₂ transforms from the 1T phase to the more stable 2H phase as growth proceeds. Notably, many defects were observed to be repaired during the phase transition process.

The growth of a second layer of MoS₂ on monolayer WS₂ was also simulated in a similar way, as shown in Fig. 1(d)-(f), which yielded similar growth pattern as observed in the growth on monolayer MoS₂. At 286.9 picoseconds, the MoS₂ layer exhibits characteristics of the 1T phase (Fig. 1e). A remarkable phenomenon observed during the growth process is the tendency of deposited Mo atoms to embed into the pre-existing WS₂ substrate. The energy barrier for Mo atoms to embed into WS₂ is relatively low, about 0.5 eV, as shown in Fig. S3. the lifetime τ of a non-embedded Mo atom on monolayer WS₂ at 1100 K was estimated to be only about 8.5 picoseconds according to transition state theory, $\frac{1}{\tau} = \frac{k_b T}{h} e^{-\frac{E_b}{k_b T}}$. That is why embedded Mo atoms were observed in our simulations. As shown in Fig. S4(a), the energy barrier for surface diffusion of embedded Mo atoms was approximately 1.75 eV, indicating that the diffusion of embedded Mo atoms on the surface was relatively difficult. This could potentially impact the stacking growth of TMDC heterostructures to some extent. Subsequently deposited S atoms were able to extract the embedded Mo atoms. As the simulation proceeds further, as illustrated in Fig. 1(f), the 2H phase of MoS₂ is finally formed on the WS₂ substrate.

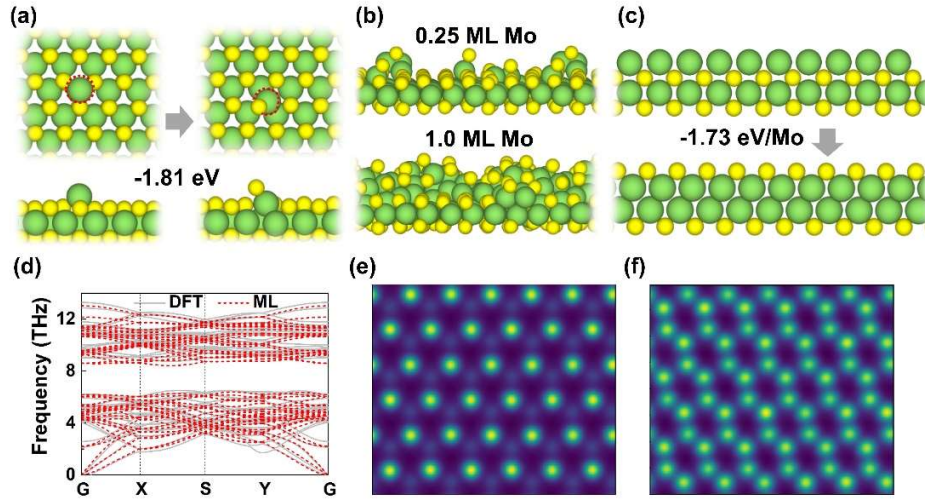


FIG. 2.: (a) Top and side views of a single Mo atom on MoS₂ surface with Mo above the S layer (left) and within the S layer (right), respectively. (b) Snapshot of the growing structure at two stages of the MLMD simulation, i.e. 0.25 monolayer (ML) Mo atoms and 1.0 ML Mo atoms on the MoS₂ substrate. (c) Schematic diagram of two possible structures of the growing system with one ML Mo atoms deposited on the MoS₂ substrate, all the deposited Mo atoms on the S layer (MoSMoS configuration) and all the deposited Mo atoms embedded underneath the S layer (SMoMoS configuration). (d) Phonon spectrum of the SMoMoS structure. Gray and red lines represent results from DFT and MLIP, respectively. (e) Simulated STEM image of the MoSMoS structure of (c) up. (f) Simulated STEM image of the SMoMoS structure (c) down.

Subsequently, we simulated the synthesis process using a two-step vapor-deposition method, in which a layer of transition metal atoms was first deposited on the TMDC substrate followed by a deposition of sulfur atoms. Our simulations were designed to replicate this process to provide insights into the atomic configurations and phase transitions that occur during the synthesis of a second MoS₂ layer on an existing MoS₂ substrate. For a single Mo atom deposited on the MoS₂ substrate, it prefers to be embedded in the S layer rather than adsorbed on the surface. The energy drop for the embedding is 1.81 eV as shown in Fig. 2(a). Over time, more and more Mo atoms are deposited to the surface. Surprisingly, these Mo atoms do not form clusters on the surface but tend to be embedded beneath the S atomic layer, as shown in Fig. 2(b) and Video S4. No Mo layer forms above S layer of the MoS₂ substrate even with one ML Mo atoms deposited. Instead, all the deposited Mo atoms tend to be embedded beneath the S layer, forming a novel SMoMoS structure, shown in Fig. 2(c). In this structure, the bottom S and Mo layers remain in their original positions from the MoS₂ structure, the upper Mo atoms occupy the positions originally held by the upper S atoms, and the upper S atoms move to the very top of the entire structure. The SMoMoS structure is 1.73 eV per Mo atom lower in energy than the MoSMoS structure. Moreover, no imaginary frequency exists in the phonon spectrum of the SMoMoS structure (Fig. 2(d)), indicating its stability. The phonon spectra obtained by DFT and MLIP are surprisingly consistent, which proves the reliability of our MLIP. The stability of this structure is further demonstrated by the NVT molecular dynamics simulation at 1100K shown in Figures S5(a) and S5(d). Therefore, we believe that the SMoMoS structure is an important intermediate state in the two-step vapor-deposition method process.

Simulated Scanning transmission electron microscopy (STEM) images for the MoSMoS and SMoMoS structures are displayed in Fig. 2(e) and 2(f). The electronic band structure of the SMoMoS intermediate state, as illustrated in Fig. S7(a), indicates that this phase exhibits metallic properties. Consequently, if the deposition of Mo atoms on the MoS₂ surface can be controlled in specific regions, it would be possible to create various electrode structures on the MoS₂ surface. This capability opens up the potential for designing spatially-resolved electronic features within a single MoS₂ sheet, enabling the fabrication of intricate circuitry and device architectures directly on the two-dimensional material.

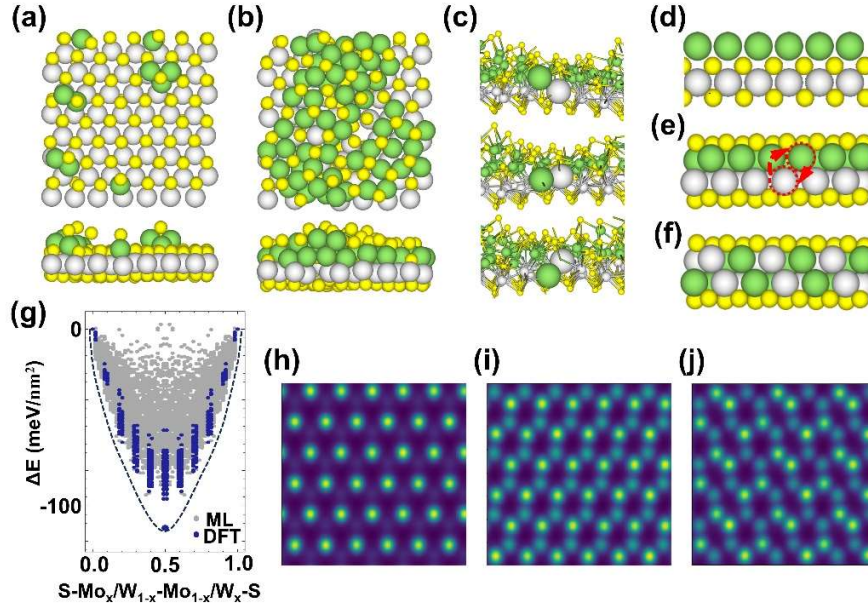


FIG. 3. (a) - (c) Snapshots of the growing structure during the two-step vapor deposition process for synthesizing the MoS₂/WS₂ heterostructure (Mo atom deposition onto WS₂). (d) Schematic of a Mo layer on the WS₂ surface. (e) Schematic of the non-alloyed S-Mo-W-S intermediate structure. (f) Schematic of an alloyed SMMS structure model. (g) Relative formation energies for different alloying ratios in the SMMS structure. (h) – (j) are simulated STEM images of (d) – (f), respectively.

The process to synthesize MoS₂/WS₂ heterostructure using a two-step vapor-deposition method was also simulated. Throughout the deposition process, the kinetic energy of the deposited atoms was ~ 0.12 eV. Like the deposition of Mo atoms on MoS₂, deposited Mo atoms are almost entirely embedded into the WS₂ substrate (shown in [Video S5](#)), no matter the amount of Mo atoms is small (Fig. 3(a)) or large (Fig. 3(b)). Fig. 3(c) shows the cross-sectional view of the evolution of the growth system over simulation time, in which the exchange of Mo and W atoms in different layers can be clearly seen. Therefore, in the actual growth process, the structure of a layer of Mo atoms on top of the WS₂ substrate shown in Fig. 3(d) would not exist. Instead, the Mo atoms would be embedded into the WS₂ substrate followed by the exchange of Mo and W atoms, as shown in Fig. 3(e). Finally, an intermediate state, i.e. an alloyed S-Metal-Metal-S (SMMS) structure, will form (Fig. 3(f)). Moreover, no imaginary frequency exists in the phonon spectrum of the SMMS structures (Fig. S6), indicating their stability. The stability of these structures are further demonstrated by the NVT molecular dynamics simulation at 1100K shown in [Figures S5](#).

To find the energy driving force for alloying, we calculated the relative energy changes ΔE for different distributions of metal atoms in the upper and lower layers. Here, ΔE is defined as $\Delta E = E - E_{SWMoS}$, where E_{SWMoS} represents the energy of the non-alloyed SMMS structure (shown in Fig. 3(d)). ΔE for SMMS structures with different alloying ratios was obtained by randomly exchanging the metal atoms in the upper and lower layers of an SMMS structure with a (7×7) supercell, followed by structural optimization. ΔE for SMMS structures with different alloying ratios is plotted in Fig. 3(j). We found that the energy is lowest when the different metal atoms are evenly distributed between the upper and lower layers, with an energy reduction of 110 meV/nm² compared to the completely non-alloyed case. Note that the lattice constant of the relaxed SMMS structure is about 5% smaller than that of the WS₂ monolayer. Consequently, when enough Mo atoms were deposited and embedded into the WS₂ substrate, the accumulated stress will lead to cracks in the bottom Metal-S layer. This cracking will facilitate the exchange of Mo and W atoms. The simulated STEM images for the structures shown in Fig. 3(d)-(f) are shown in Fig. 3(g)-(i), to visualize the impact of alloying. The non-alloyed and alloyed SMMS structures are both metallic and the alloying has little effect on the electronic band structure as shown in Fig. S7(b).

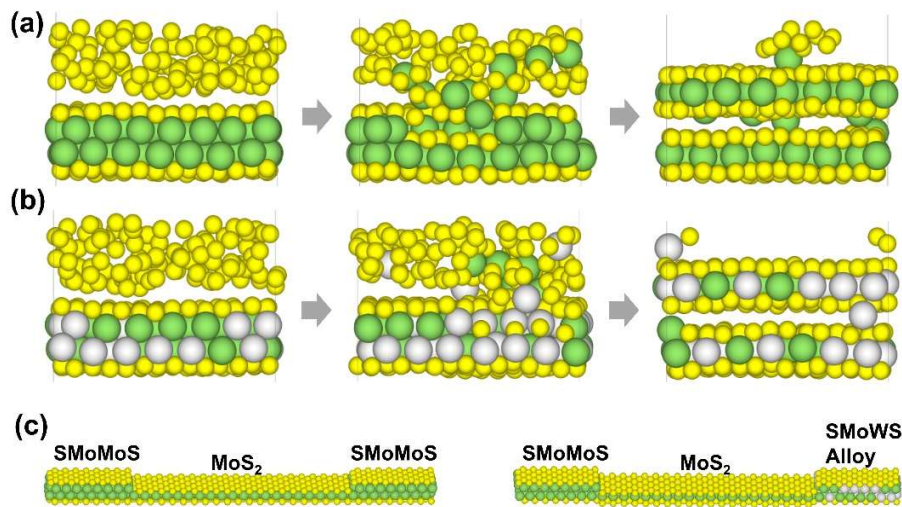


FIG. 4. (a) MLMD simulation of the growth of bilayer MoS₂ structure by depositing S atoms on the SMOsMoS intermediate phase. (b) MLMD simulation of the growth of alloyed Mo_xW_{1-x}S₂/Mo_{1-x}W_xS₂ heterostructure by depositing S atoms on the alloyed SMMS intermediate phase. (c) Schematic representation of an FET based on TMDC with self-intercalating SMMS electrodes.

The transformation from the intermediate phase to heterostructure in the two-step vapor-deposition method was further investigated by MLMD simulations with MLIP. For the growth of bilayer MoS₂, the MLMD starts with proper amount of S atoms randomly distributed on top of SMOsMoS intermediate phase as shown in Fig. 4(a) and Video S6. Over time, we can see that some S atoms penetrate the SMOsMoS structure and pull some Mo atoms to the surface. Finally, a MoS₂ bilayer forms. Similarly, for the growth of MoS₂/WS₂ heterostructure, the MLMD starts with proper amount of S atoms randomly distributed on top of alloyed SMMS intermediate phase as shown in Fig. 4(b) and Video S7. As time goes by, S atoms start to penetrate the SMMS structure and pull some Mo and W atoms to the surface. Finally, a Mo_xW_{1-x}S₂/Mo_{1-x}W_xS₂ heterostructure forms instead of a MoS₂/WS₂ heterostructure. If the deposition of S atoms can be well controlled, a self-intercalating electrode for transition metal dichalcogenides based FET can be designed utilizing the metallic nature of the SMMS structure as shown in figures 4(c).

In summary, we have developed a MLIP to describe the stacking growth of TMDCs. This potential function accurately characterizes the complex stacking growth of TMDCs and the recently advanced two-step vapor-deposition method. Furthermore, a novel structure of SMMS was proposed, which is a potential intermediate state during the two-step vapor-deposition process and plays an important role in the growth of TMDCs. The SMMS also provides a novel way for electrode design in TMDC-based devices. Our results provide deep insights into the intricate atomic movements and phase transitions that occur during the growth process of bilayer TMDC or TMDC heterostructure.

Reference

- [1] Z. Wang, C.-Y. Cheon, M. Tripathi, G. M. Marega, Y. Zhao, H. G. Ji, M. Macha, A. Radenovic, and A. Kis, *Superconducting 2D NbS₂ Grown Epitaxially by Chemical Vapor Deposition*, ACS Nano **15**, 18403 (2021).
- [2] Y. K. Srivastava, A. Chaturvedi, M. Manjappa, A. Kumar, G. Dayal, C. Kloc, and R. Singh, *MoS₂ for Ultrafast All-Optical Switching and Modulation of THz Fano Metaphotonic Devices*, Advanced Optical Materials **5**, 1700762 (2017).
- [3] R. Feng et al., *Selective Control of Phases and Electronic Structures of Monolayer TaTe₂*, Advanced Materials **36**, 2302297 (2024).
- [4] H. Habib, W. Zhao, S. Mir, L. Ma, and G. Tian, *First-Principles Studies on the Structural, Electronic, and Optical Properties of 2D Transition Metal Dichalcogenide (TMDC) and Janus TMDCs Heterobilayers*, J. Phys.: Condens. Matter **35**, 505501 (2023).
- [5] D. Andrzejewski, H. Myja, M. Heuken, A. Grundmann, H. Kalisch, A. Vescan, T. Kümmell, and G. Bacher, *Scalable Large-Area pin Light-Emitting Diodes Based on WS₂ Monolayers Grown via MOCVD*, ACS Photonics **6**, 1832 (2019).
- [6] Y. Kobayashi, S. Yoshida, M. Maruyama, H. Mogi, K. Murase, Y. Maniwa, O. Takeuchi, S. Okada, H. Shigekawa, and Y. Miyata, *Continuous Heteroepitaxy of Two-Dimensional Heterostructures Based on Layered Chalcogenides*, ACS Nano **13**, 7527 (2019).

- [7] A. T. Hoang, K. Qu, X. Chen, and J.-H. Ahn, *Large-Area Synthesis of Transition Metal Dichalcogenides via CVD and Solution-Based Approaches and Their Device Applications*, *Nanoscale* **13**, 615 (2021).
- [8] S.-S. Chee, W.-J. Lee, Y.-R. Jo, M. K. Cho, D. Chun, H. Baik, B.-J. Kim, M.-H. Yoon, K. Lee, and M.-H. Ham, *Atomic Vacancy Control and Elemental Substitution in a Monolayer Molybdenum Disulfide for High Performance Optoelectronic Device Arrays*, *Adv Funct Materials* **30**, 1908147 (2020).
- [9] T. Ahmed, J. Zha, K. K. Lin, H.-C. Kuo, C. Tan, and D.-H. Lien, *Bright and Efficient Light-Emitting Devices Based on 2D Transition Metal Dichalcogenides*, *Advanced Materials* **35**, 2208054 (2023).
- [10] H. G. Ji, P. Solís-Fernández, D. Yoshimura, M. Maruyama, T. Endo, Y. Miyata, S. Okada, and H. Ago, *Chemically Tuned p- and n-Type WSe₂ Monolayers with High Carrier Mobility for Advanced Electronics*, *Advanced Materials* **31**, 1903613 (2019).
- [11] S. Wang, H. Sawada, C. S. Allen, A. I. Kirkland, and J. H. Warner, *Orientation Dependent Interlayer Stacking Structure in Bilayer MoS₂ Domains*, *Nanoscale* **9**, 13060 (2017).
- [12] I. Niehues, A. Blob, T. Stiehm, R. Schmidt, V. Jadriško, B. Radatović, D. Čapeta, M. Kralj, S. M. De Vasconcellos, and R. Bratschitsch, *Strain Transfer Across Grain Boundaries in MoS₂ Monolayers Grown by Chemical Vapor Deposition*, *2D Mater.* **5**, 031003 (2018).
- [13] W. T. Kang et al., *Direct Growth of Doping Controlled Monolayer WSe₂ by Selenium-Phosphorus Substitution*, *Nanoscale* **10**, 11397 (2018).
- [14] Y. Gong et al., *Vertical and in-Plane Heterostructures from WS₂/MoS₂ Monolayers*, *Nature Mater* **13**, 1135 (2014).
- [15] X. Jiang, F. Chen, S. Zhao, and W. Su, *Recent Progress in the CVD Growth of 2D Vertical Heterostructures Based on Transition-Metal Dichalcogenides*, *CrystEngComm* **23**, 8239 (2021).
- [16] F. Ullah et al., *Growth and Simultaneous Valleys Manipulation of Two-Dimensional MoSe₂-WSe₂ Lateral Heterostructure*, *ACS Nano* **11**, 8822 (2017).
- [17] S. H. Choi et al., *Epitaxial Single-Crystal Growth of Transition Metal Dichalcogenide Monolayers via the Atomic Sawtooth Au Surface*, *Advanced Materials* **33**, 2006601 (2021).
- [18] W. Yang et al., *Interlayer Interactions in 2D WS₂/MoS₂ Heterostructures Monolithically Grown by in Situ Physical Vapor Deposition*, *Nanoscale* **10**, 22927 (2018).
- [19] Y. Shi, H. Zhang, W.-H. Chang, H. S. Shin, and L.-J. Li, *Synthesis and Structure of Two-Dimensional Transition-Metal Dichalcogenides*, *MRS Bull.* **40**, 566 (2015).
- [20] Q. An, T. Zhang, F. Chen, and W. Su, *Recent Progress in the Synthesis and Physical Properties of 2D Ternary TMDC-based Vertical Heterostructures*, *CrystEngComm* **25**, 4256 (2023).
- [21] M.-Y. Li et al., *Epitaxial Growth of a Monolayer WSe₂-MoS₂ Lateral p-n Junction with an Atomically Sharp Interface*, (n.d.).
- [22] Z. Zhang, Y. Gong, X. Zou, P. Liu, P. Yang, J. Shi, L. Zhao, Q. Zhang, L. Gu, and Y. Zhang, *Epitaxial Growth of Two-Dimensional Metal (VSe₂/MX₂) and Their Band Alignments*, *ACS Nano* **13**, 885 (2019).
- [23] Y. Yoo, Z. P. Degregorio, and J. E. Johns, *Seed Crystal Homogeneity Controls Lateral and Vertical Heteroepitaxy of Monolayer MoS₂ and WS₂*, *J. Am. Chem. Soc.* **137**, 14281 (2015).
- [24] G. Jin et al., *Heteroepitaxial van Der Waals Semiconductor Superlattices*, *Nat. Nanotechnol.* **16**, 1092 (2021).
- [25] J. Wang, T. Li, Q. Wang, W. Wang, R. Shi, N. Wang, A. Amini, and C. Cheng, *Controlled Growth of Atomically Thin Transition Metal Dichalcogenides via Chemical Vapor Deposition Method*, *Materials Today Advances* **8**, 100098 (2020).
- [26] C. B. López-Posadas, Y. Wei, W. Shen, D. Kahr, M. Hohage, and L. Sun, *Direct Observation of the CVD Growth of Monolayer MoS₂ Using in Situ Optical Spectroscopy*, *Beilstein J. Nanotechnol.* **10**, 557 (2019).
- [27] C. K. Kanade, H. Seok, V. K. Kanade, K. Aydin, H.-U. Kim, S. B. Mitta, W. J. Yoo, and T. Kim, *Low-Temperature and Large-Scale Production of a Transition Metal Sulfide Vertical Heterostructure and Its Application for Photodetectors*, *ACS Appl. Mater. Interfaces* **13**, 8710 (2021).
- [28] J. Wang, T. Li, Q. Wang, W. Wang, R. Shi, N. Wang, A. Amini, and C. Cheng, *Controlled Growth of Atomically Thin Transition Metal Dichalcogenides via Chemical Vapor Deposition Method*, *Materials Today Advances* **8**, 100098 (2020).

- [29] Y. Wang, M. Nakano, Y. Kashiwabara, H. Matsuoka, and Y. Iwasa, *Transport Properties of a Few Nanometer-Thick TiSe₂ Films Grown by Molecular-Beam Epitaxy*, Applied Physics Letters **113**, 073101 (2018).
- [30] B. Wang, Y. Xia, J. Zhang, H.-P. Komsa, M. Xie, Y. Peng, and C. Jin, *Niobium Doping Induced Mirror Twin Boundaries in MBE Grown WSe₂ Monolayers*, Nano Res. **13**, 1889 (2020).
- [31] S. J. McDonnell and R. M. Wallace, *Atomically-Thin Layered Films for Device Applications Based Upon 2D TMDC Materials*, Thin Solid Films **616**, 482 (2016).
- [32] Z. Zhou et al., *Stack Growth of Wafer-Scale van Der Waals Superconductor Heterostructures*, Nature **621**, 499 (2023).
- [33] G. P. P. Pun, R. Batra, R. Ramprasad, and Y. Mishin, *Physically Informed Artificial Neural Networks for Atomistic Modeling of Materials*, Nat Commun **10**, 2339 (2019).
- [34] J. Zeng, L. Cao, M. Xu, T. Zhu, and J. Z. H. Zhang, *Complex Reaction Processes in Combustion Unraveled by Neural Network-based Molecular Dynamics Simulation*, Nat Commun **11**, 5713 (2020).
- [35] L. Hu, B. Huang, and F. Liu, *Atomistic Mechanism Underlying the Si (111) - (7 7) Surface Reconstruction Revealed by Artificial Neural-network Potential*, Phys. Rev. Lett. **126**, 176101 (2021).
- [36] T. Morawietz and N. Artrith, *Machine Learning-Accelerated Quantum Mechanics-Based Atomistic Simulations for Industrial Applications*, J Comput Aided Mol Des **35**, 557 (2021).
- [37] O. T. Unke, S. Chmiela, H. E. Sauceda, M. Gastegger, I. Poltavsky, K. T. Schütt, A. Tkatchenko, and K.-R. Müller, *Machine Learning Force Fields*, Chem. Rev. **121**, 10142 (2021).
- [38] K. Momeni et al., *Multiscale Computational Understanding and Growth of 2D Materials: A Review*, Npj Comput Mater **6**, 22 (2020).
- [39] J. Zhang, F. Wang, V. B. Shenoy, M. Tang, and J. Lou, *Towards Controlled Synthesis of 2D Crystals by Chemical Vapor Deposition (CVD)*, Materials Today **40**, 132 (2020).
- [40] B. Deng, P. Zhong, K. Jun, J. Riebesell, K. Han, C. J. Bartel, and G. Ceder, *CHGNet as a Pretrained Universal Neural Network Potential for Charge-Informed Atomistic Modelling*, Nat Mach Intell **5**, 1031 (2023).
- [41] B. Lin, J. Jiang, X. C. Zeng, and L. Li, *Temperature-Pressure Phase Diagram of Confined Monolayer Water/Ice at First-Principles Accuracy with a Machine-Learning Force Field*, Nat Commun **14**, 4110 (2023).
- [42] S. Batzner, A. Musaelian, L. Sun, M. Geiger, J. P. Mailoa, M. Kornbluth, N. Molinari, T. E. Smidt, and B. Kozinsky, *E(3)-Equivariant Graph Neural Networks for Data-efficient and Accurate Interatomic Potentials*, Nat Commun **13**, 2453 (2022).
- [43] M. A. Caro, V. L. Deringer, J. Koskinen, T. Laurila, and G. Csányi, *Growth Mechanism and Origin of High *s p*³ Content in Tetrahedral Amorphous Carbon*, Phys. Rev. Lett. **120**, 166101 (2018).
- [44] M. A. Caro, G. Csányi, T. Laurila, and V. L. Deringer, *Machine Learning Driven Simulated Deposition of Carbon Films: From Low-Density to Diamondlike Amorphous Carbon*, Phys. Rev. B **102**, 174201 (2020).
- [45] J. Jiao et al., *Self-Healing Mechanism of Lithium in Lithium Metal*, Advanced Science **9**, 2105574 (2022).
- [46] D. Dragoni, J. Behler, and M. Bernasconi, *Mechanism of Amorphous Phase Stabilization in Ultrathin Films of Monoatomic Phase Change Material*, Nanoscale **13**, 16146 (2021).
- [47] W. Liu, Y. Zhu, Y. Wu, C. Chen, Y. Hong, Y. Yue, J. Zhang, and B. Hou, *Molecular Dynamics and Machine Learning in Catalysts*, Catalysts **11**, 1129 (2021).